photonics

MDPI

Article

Effect of Graphene Oxide on the Structural and Optical Properties of FTO Layers Obtained by Spray Pyrolysis

Pavel Parchinsky [1,*], Abdumanap A. Nasirov [1], Shavkat U. Yuldashev [1], Azamat Arslanov [1], Rafael A. Nusretov [2], Natalia A. Kulagina [3], Sultan Kh. Suleymanov [3], Peng Li [4], Sergei A. Khakhomov [5], Alina V. Semchenko [5], Vitali V. Sidski [5], Vladimir E. Gaishun [5] and Konstantin D. Danilchenko [5]

[1] Department of Semiconductors and Polymers Physics, National University of Uzbekistan, 4 University Street, Tashkent 100174, Uzbekistan; aanasirov1962@mail.ru (A.A.N.); yuldashev_sh@nuu.uz (S.U.Y.); arslonov_a@nuu.uz (A.A.)
[2] Uzbek–Japanese Youth Center for Innovations, 17a Shakhrisabz Street, Tashkent 100095, Uzbekistan; rnusretov@yandex.ru
[3] Institute of Materials Science, Academy of Sciences of the Republic of Uzbekistan, 2b Chingiz Aytmatov Street, Tashkent 100084, Uzbekistan; n.kulagina@imssolar.uz (N.A.K.); s.suleymanov@imssolar.uz (S.K.S.)
[4] School of Microelectronics, University of Science and Technology of China, 96 Jinzhai Road, Hefei 230026, China; lipeng18@ustc.edu.cn
[5] Faculty of Physics and IT, Francisk Skorina Gomel State University, 104 Sovetskaya Street, 246019 Gomel, Belarus; khakh@gsu.by (S.A.K.); semchenko@gsu.by (A.V.S.); sidsky@gsu.by (V.V.S.); vgaishun@gsu.by (V.E.G.); konstantindmitrievich1996@gsu.by (K.D.D.)
* Correspondence: pavelphys@mail.ru; Tel.: +998-93-540-57-59

Abstract

This study examines the effect of graphene oxide nanoparticle (NGO) doping (0.12–0.24 mol%) on the properties of FTO layers obtained by spray pyrolysis. The results show that nanographene promotes phase separation within the FTO bulk. The resulting inhomogeneities are fluorine-depleted relative to the surrounding film. NGO doping also modifies the position and intensity of peaks in the absorption spectra, indicating a change in the nature of the absorbing centers. The optical bandgap of the FTO layers decreases with the increase in NGO from 4.4 eV (undoped samples) to 3.95 eV (samples with the highest NGO concentration). Furthermore, NGO doping reduces the sheet resistance of the FTO layers. This reduction is attributed to increased charge carrier mobility resulting from passivation of nanocrystallite interfaces by graphene oxide nanoparticles. However, the sheet resistance depends non-monotonically on NGO content, with the lowest value observed at 0.16 mol% NGO. The increase in resistance at higher NGO concentrations is due to enhanced carrier scattering caused by the growing size and number of the phase inhomogeneities within the FTO layer.

Keywords: FTO (fluorine-doped tin oxide); graphene oxide; spray pyrolysis; transparent conducting oxides; phase separation; optical bandgap; sheet resistance; structural properties; co-doping; nanographene

Check for updates

Received: 7 July 2026
Revised: 30 July 2026
Accepted: 31 July 2026
Published: 22 August 2026

Copyright: © 2026 by the authors. Licensee MDPI, Basel, Switzerland. This article is an open access article distributed under the terms and conditions of the Creative Commons Attribution (CC BY) license.

1. Introduction

Transparent conducting oxides are currently widely used in various fields of electronics, optoelectronics, and photovoltaics [1–5]. From a practical perspective, indium tin oxide (ITO) appears to be the most promising material, as it offers the best combination of high transparency and low resistivity among transparent conducting oxides [6,7]. However, its widespread application is limited by the high cost of indium, since achieving the desired

optical and electrophysical properties requires an indium oxide content of at least 90 wt% in ITO [8,9]. Among the materials considered as ITO substitutes, fluorine-doped tin oxide (F-doped SnO_2 or FTO) attracts the greatest attention [10,11]. This material is almost comparable to ITO in terms of its optical properties. At the same time, it has low cost and high technological availability. Furthermore, FTO films are thermally stable up to 300 °C and exhibit high resistance to aggressive chemical environments. This makes them suitable as substrates for the synthesis of active layers in various devices and structures of transparent electronics and photovoltaics [12,13].

Another advantage of FTO films is the ability to adjust their work function and bandgap over a relatively wide range [12,14,15]. This capability allows optimization of the potential barrier height between the FTO film and the active region of a solar cell, making FTO films promising as conductive collecting electrodes (electron transport layers) in solar cells [5,16].

At the same time, FTO films are inferior to ITO films in terms of conductivity, which can adversely affect the characteristics of devices and structures utilizing them. Notably, FTO films prepared by physical and chemical deposition methods have a micro- and nanocrystalline structure. Their conductivity is determined both by the concentration of donor centers (interstitial Sn atoms, oxygen vacancies, and fluorine atoms in the oxygen sublattice) and by effects at crystallite interfaces [17,18]. Consequently, conductivity depends on both the composition and the structure of the film. Thus, obtaining FTO films with the desired electrophysical characteristics is possible by selecting the optimal composition, deposition conditions, and subsequent thermal treatments [12,19,20]. Another approach to increasing the conductivity of FTO films involves doping with various impurities that elevate the donor concentration within the bandgap [5,21,22]. To date, it has been shown that introducing carbon nanostructures (fullerenes, nanotubes, and graphene) into the bulk of conducting oxides could significantly modify their structural and electrophysical properties [22–27]. Specifically, studies [22,25–27] have demonstrated that doping with graphene and its derivatives can positively influence the optical and transport properties of FTO.

The choice of graphene oxide nanoparticles (NGOs) as a doping agent for the FTO system is motivated by several complementary factors. First, the two-dimensional structure and high specific surface area of graphene-based materials provide an extended interface for interaction with the developing oxide matrix and may influence charge-transport pathways in transparent conducting oxides. Second, the oxygen-containing functional groups present on the NGO surface facilitate its dispersion in the water–alcohol media commonly used for sol–gel-based precursor systems, which is particularly important for obtaining reproducible coatings by spray pyrolysis. Third, previous studies [22,25–27] have demonstrated that graphene-based additives can improve the electrical and optical characteristics of FTO films, although the mechanisms responsible for these effects remain insufficiently understood. Compared with other carbon-based nanomaterials, the functionalized surface of NGOs provides additional opportunities for interaction with the oxide precursor and the developing SnO_2-based matrix. This makes NGOs a suitable model nanocarbon additive for investigating the relationship between carbon modification, local structural and compositional heterogeneity, and the resulting optical and electrical properties of FTO films. At the same time, the ability to control the NGO concentration provides a practical approach for tuning the performance of transparent conducting layers. Nevertheless, we still have a limited understanding of how carbon nanostructures influence the characteristics of FTO layers.

Considering the aforementioned points, investigating the doping of FTO with graphene oxide to obtain thin films with tailored properties for optoelectronic and photo-

voltaic applications is a relevant task. This paper presents the findings of a study examining the effect of graphene oxide nanoparticle (NGO) concentration on the structural, optical, and electrophysical parameters of FTO layers deposited via ultrasonic spray pyrolysis.

2. Samples and Measurement Techniques

2.1. Sample Fabrication

Transparent conducting films composed of fluorine-doped tin oxide (FTO) and those doped with NGOs with a thickness of 50 nm were prepared by spray pyrolysis using sol–gel technology. This approach enables the formation of uniform coatings on large-area substrates without requiring vacuum equipment.

The layers under study were grown on p-type silicon substrates with a resistivity of 4 Ω·cm. A water–alcohol sol was prepared for the formation of the FTO layers. Hydrolysis of the solutions was performed in a water–alcohol medium using ethyl alcohol as the solvent. Tin chloride and ammonium fluoride of ultrapure grade were selected as starting materials. A solution containing NGO powder (commercially available aqueous dispersion of graphene oxide with an average particle size of 50 nm, manufactured by Ecoteck (Russian Federation) at a concentration of 2 mol%) was added into the obtained sol. The initial NGO powder was characterized by dynamic light scattering (DLS) using a Zetasizer Nano ZS instrument and by transmission electron microscopy (Malvern Panalytical Zetasizer, TEM-120, EMTION). The average hydrodynamic diameter of the nanoparticles in the water–alcohol suspension was 48 ± 5 nm. To reduce the formation of agglomerates before mixing with the sol–gel solution, the suspension was treated using an ultrasonic disperser (UZDN-2T, 44 kHz, 50 W) for 30 min. After incorporation into the main precursor solution, a second ultrasonic treatment was performed for 20 min. The particle size in the final suspension was subsequently re-evaluated by DLS, and the average particle size remained within the range of 50–55 nm, indicating the absence of significant aggregation during preparation. In addition, the presence of nanoparticles in the deposited films was confirmed by TEM analysis of cross-sectional specimens, and the particle sizes observed in the films were consistent with those determined in the precursor suspension. The concentration of the NGO solution in the initial sol ranged from 6 to 12 mol%. Thus, the final nanographene concentration in the samples ranged from 0.12 to 0.24 mol%. The samples were designated according to the nanographene solution content in the initial sol: FTO-0 (control sample, devoid of nanographene) and FTO-6 to FTO-12 (samples containing 6 to 12 mol% of nanographene solution in the initial sol, respectively).

The resulting mixture underwent treatment in an ultrasonic bath until complete dissolution of the components. To break down agglomerates and ensure uniform particle distribution, the NGO-containing solutions were additionally treated with ultrasound. Thereafter, all solutions were kept at room temperature (22 ± 2 °C) for 2–3 days to complete the hydrolysis processes and establish a stable sol.

The films were deposited using a spray pyrolysis setup with pneumatic atomization (Figure 1). Cleaned Si substrates were fixed horizontally in the reaction chamber and heated to 450–550 °C. For solution atomization, a compressor-driven jet nebulizer was employed; the sol was converted into a fine aerosol by compressed air at a pressure of about 2 atm. The aerosol stream was directed onto the heated substrate, where pyrolytic decomposition of the salts occurred, forming the FTO film. Volatile reaction products and solvent residues were removed in the vapor phase. The vertical positioning of the substrate improved the uniformity of the resulting coatings. Optimization of the deposition parameters was performed in several stages. During the preliminary optimization stage, the substrate temperature was varied from 400 to 600 °C in 25 °C increments, while the atomizing gas pressure and solution feed rate were varied within the ranges of 1–3 atm and 1–5 mL/min,

respectively. The optimization criteria were the minimum sheet resistance, determined using the four-probe method, and the maximum optical transmittance in the visible spectral range, determined by spectrophotometry. Based on these criteria, a substrate temperature of 480 °C, an atomizing gas pressure of 2 atm, and a solution feed rate of 3 mL/min were selected as the optimal deposition conditions for the undoped FTO films. The fluorine concentration in the precursor solution, expressed as the NH_4F-to-$SnCl_2$ molar ratio, was optimized separately and fixed at 10 mol%, in accordance with the literature data [11,20]. For each set of deposition conditions, at least three samples were prepared to evaluate the reproducibility of the results. The NGO concentration was subsequently varied in the range of 0.12–0.24 mol% based on preliminary experiments. Lower NGO concentrations produced no pronounced changes in the electrical properties, whereas higher concentrations resulted in increased particle aggregation and deterioration of the film morphology. The spraying process continued until the desired film thickness was achieved, following which the samples were cooled in air.

2.2. Measurement Techniques

Surface morphology of the samples was examined using a JEOL JSM IT 200 scanning electron microscope equipped with an energy-dispersive X-ray spectrometer (EDS) for chemical composition analysis. X-ray diffraction (XRD) analysis was performed using an Empyrean diffractometer (Malvern Panalytical) equipped with software for crystal lattice parameter identification. Absorption spectra in the range of 150–900 nm were recorded using a YOKE M601S-x spectrophotometer. The optical bandgap of the analyzed layers was determined from the absorption spectra using the Tauc method. Sheet resistance (R_{sheet}) of the studied samples was measured in the dark at room temperature using the four-probe method with a setup based on a Keithley 2805 source measure unit. As the conductivity of Si substrate is opposite to the conductivity of FTO films, a p–n junction was formed at the FTO–Si interface, preventing current leakage into the silicon substrate during sheet resistance measurement.

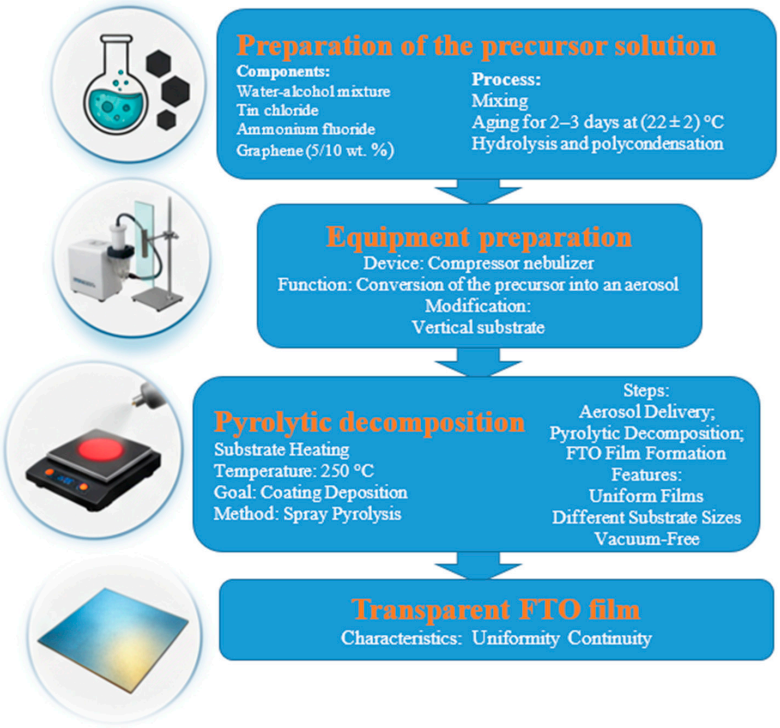


Figure 1. Procedure for the fabrication of FTO films via spray pyrolysis.

3. Results and Discussion

Figure 2a–e present scanning electron microscopy images of the surface of FTO layers with different NGO contents. Surface relief inhomogeneities are observed on the film surfaces, with both their concentration and size increasing with increase in NGO content. Specifically, in the FTO-12 layers (with the highest NGO content), the number of inhomogeneities per unit surface area exceeds the number in the nanographene-free layers by a factor of 2–2.5, while their average diameter increases from 8–10 μm to 20–25 μm. This suggests that introducing NGO into FTO films during synthesis stimulates the phase separation processes.

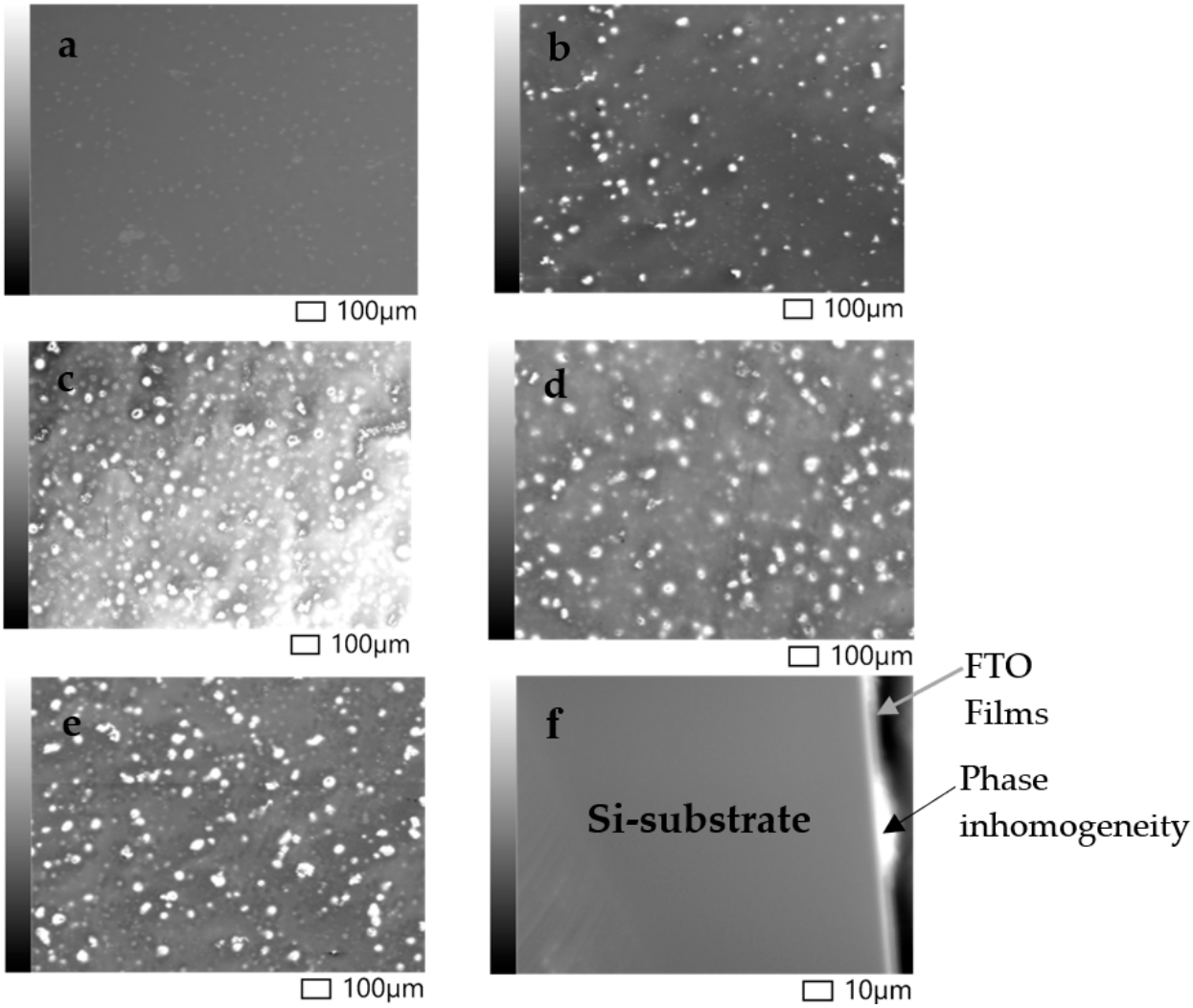


Figure 2. Scanning electron microscopy images depicting the surface of FTO layers doped with nanographene: (**a**) FTO-0; (**b**) FTO-6; (**c**) FTO-8; (**d**) FTO-10; (**e**) FTO-12; (**f**) image of cross-sectional cleavage passing through a phase inhomogeneity in the FTO-12 sample.

Figure 2f shows an image of a cross-sectional cleavage passing through a phase inhomogeneity in the FTO-12 sample. The inhomogeneity extends through the entire film thickness and is 3–3.5 times thicker than the surrounding film.

To determine the composition of the observed phase inhomogeneities, elemental analysis of the FTO films was performed using energy-dispersive X-ray spectroscopy (EDS). Figure 3 presents the EDS mapping results for the FTO-10 sample. The inhomogeneities differ in composition from the bulk film. Specifically, the tin and oxygen line intensities increase in the inhomogeneity regions, while the fluorine line intensity remains constant.

Table 1 lists the elemental composition (mass and atomic fractions) of the samples, averaged over the entire film surface shown in the image and the composition measured at a phase inhomogeneity point. The data for the phase inhomogeneity composition are averaged over five different points.

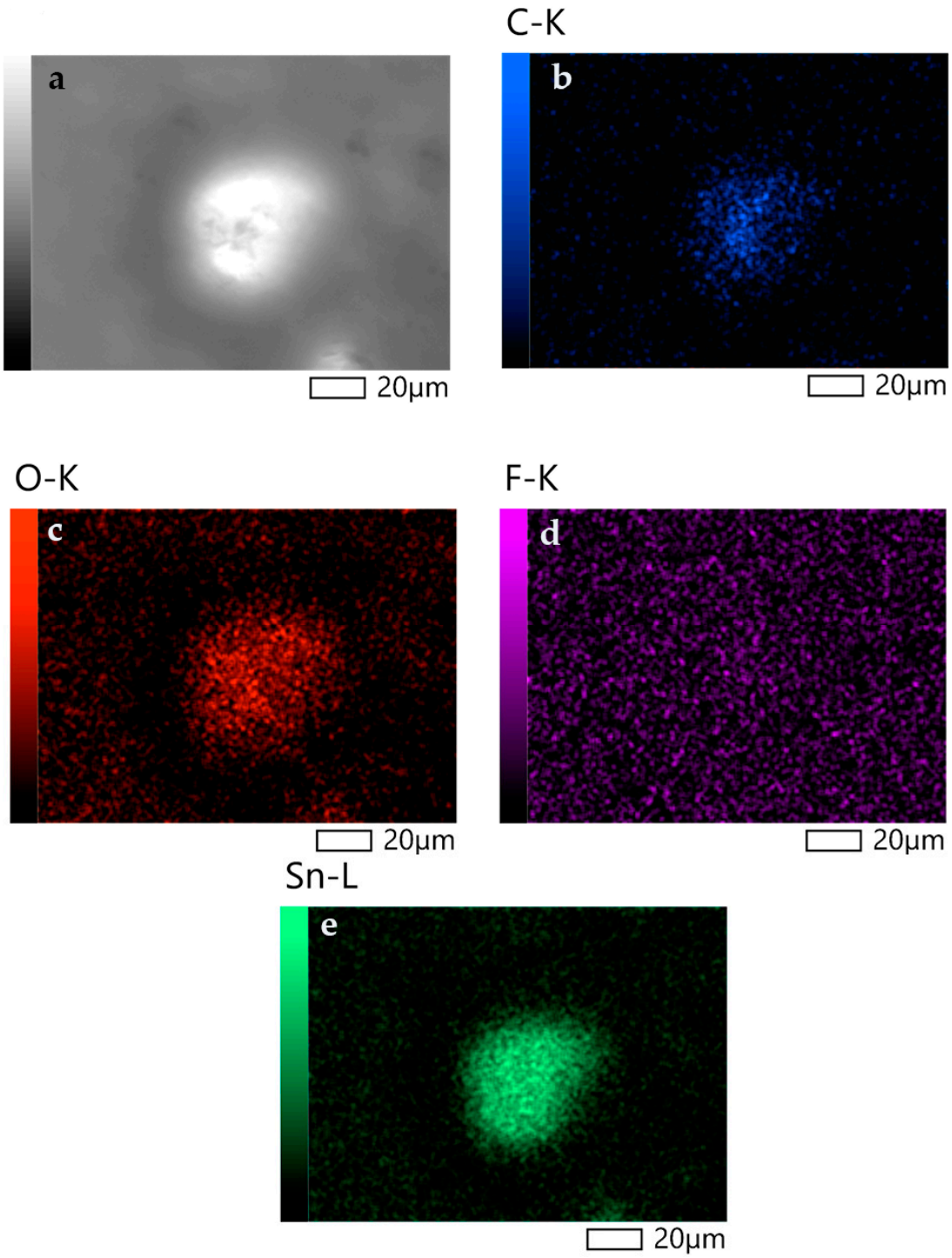


Figure 3. (**a**) Phase inhomogeneity image of the FTO-10 film; (**b**–**e**) EDS mapping results of the same region.

Table 1. Elemental composition of the FTO-10 film as per EDS mapping data.

Element	Surface-Averaged Value		Value at the Phase Inhomogeneity Point	
	Mass%	at.%	Mass%	at.%
C	6.23 ± 0.02	12.36 ± 0.05	6.23 ± 0.02	12.88 ± 0.04
O	52.21 ± 0.18	77.78 ± 0.27	49.39 ± 0.16	76.70 ± 0.25
F	1.44 ± 0.09	1.80 ± 0.11	1.03 ± 0.07	1.35 ± 0.09
Sn	40.12 ± 0.12	8.06 ± 0.02	43.35 ± 0.11	9.07 ± 0.02

The results presented in Table 1 indicate that the inhomogeneities are enriched with tin and depleted with fluorine, confirming the EDS mapping data. A slight increase in carbon concentration is also observed within the phase inhomogeneities. However, a carbon background of 12–14 at.% is present in the analyzed films, associated with traces of organic compounds used in the film synthesis. This background prevents a definitive conclusion on whether the increased EDS signal intensity in the inhomogeneities is due to a higher nanographene content. Alternatively, it may simply result from the larger interaction volume (greater thickness) of inhomogeneity regions.

Figure 4 presents linear EDS mapping data for NGO-containing samples along lines passing through phase inhomogeneities. Tin enrichment of the phase inhomogeneities relative to the film composition is observed in all NGO-containing samples according to obtained data.

Figure 5 presents X-ray diffraction (XRD) data for NGO-containing FTO films. The reflections observed in the XRD spectra and parameters of crystalline lattice were identified automatically, using the Empyrean diffractometer database and reference works [28–33]. The parameters of the crystalline phases of the NGO-containing FTO layers are summarized in Table 2, with reflection positions provided only for the most intense peaks: (110), (101), and (211). The data reveal the presence of two crystalline phases of tin oxide in the analyzed films. Both phases belong to space group $P4_2/mnm$ but are characterized by different lattice parameters and unit cell volumes.

Table 2. Parameters of the crystalline phases of FTO layers doped with NGOs. Indices 1 and 2 refer to the phases with larger and smaller unit cell volumes, respectively.

Parameter	FTO-6	FTO-8	FTO-10	FTO-12
Preferred crystallographic plane	101	110	110	101
Reflection position for (110), phase 1	26.291	26.487	26.325	26.487
Reflection position for (110), phase 2 [$^0 2\Omega$]	26.717	26.585	26.888	27.076
Reflection position for (101), phase 1 [$^0 2\Omega$]	33.663	33.740	33.550	33.740
Reflection position for (101), phase 2 [$^0 2\Omega$]	33.871	34.405	34.137	34.291
Reflection position for (211), phase 1	51.287	51.564	51.245	51.564
Reflection position for (211), phase 2	51.919	52.149	52.304	52.627
a_1	4.7900	4.7552	4.7840	4.7552
a_2	4.7150	4.7380	4.6855	4.6537
c_1	3.1990	3.1992	3.2160	3.1992
c_2	3.1940	3.1180	3.1679	3.1577
V_1/V_2	73.40/71.01	72.34/69.99	73.60/69.55	72.34/68.39

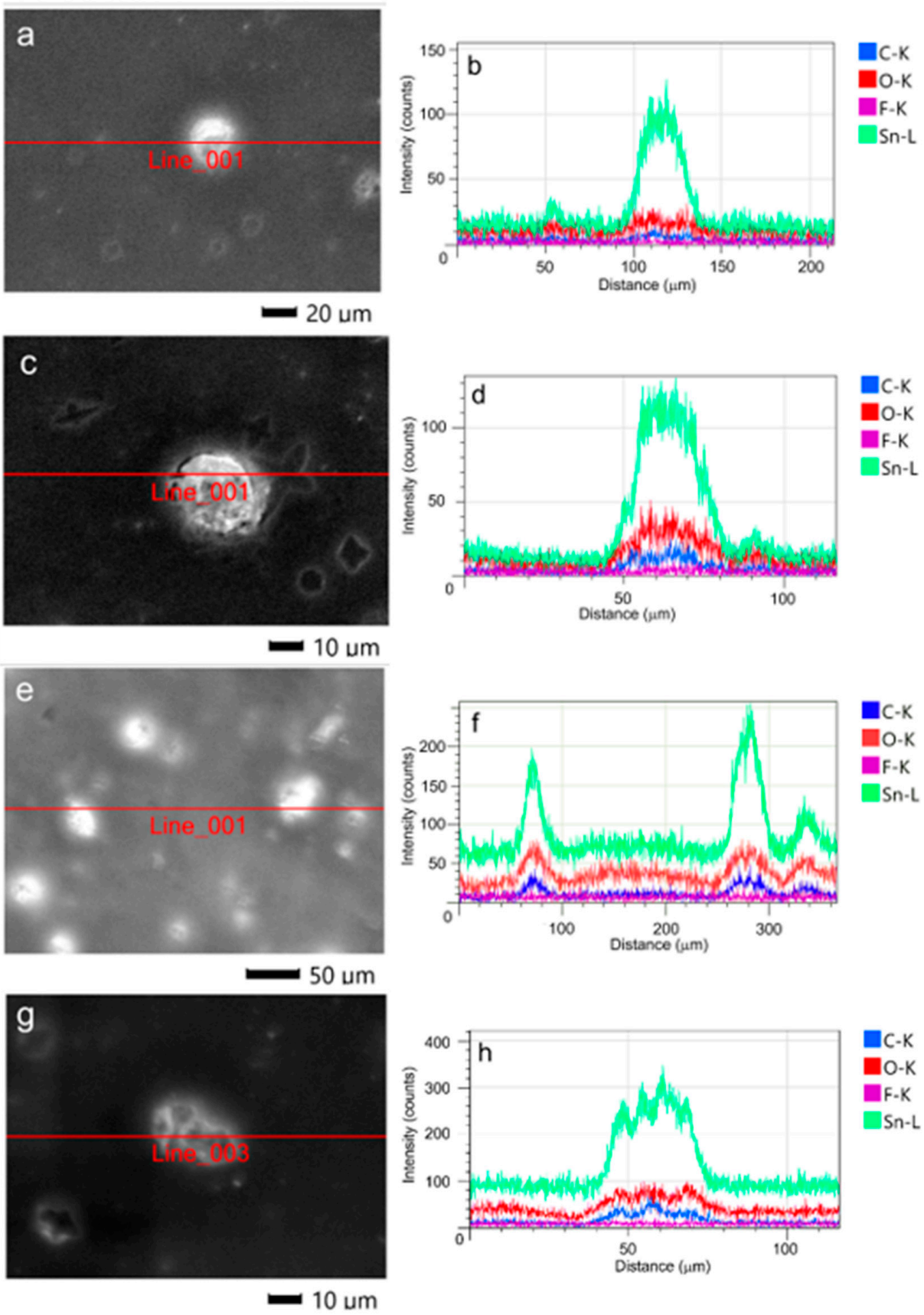


Figure 4. Linear EDS mapping data for NGO-containing samples: (**a**,**b**) FTO-6; (**c**,**d**) FTO-8; (**e**,**f**) FTO-10; (**g**,**h**) FTO-12.

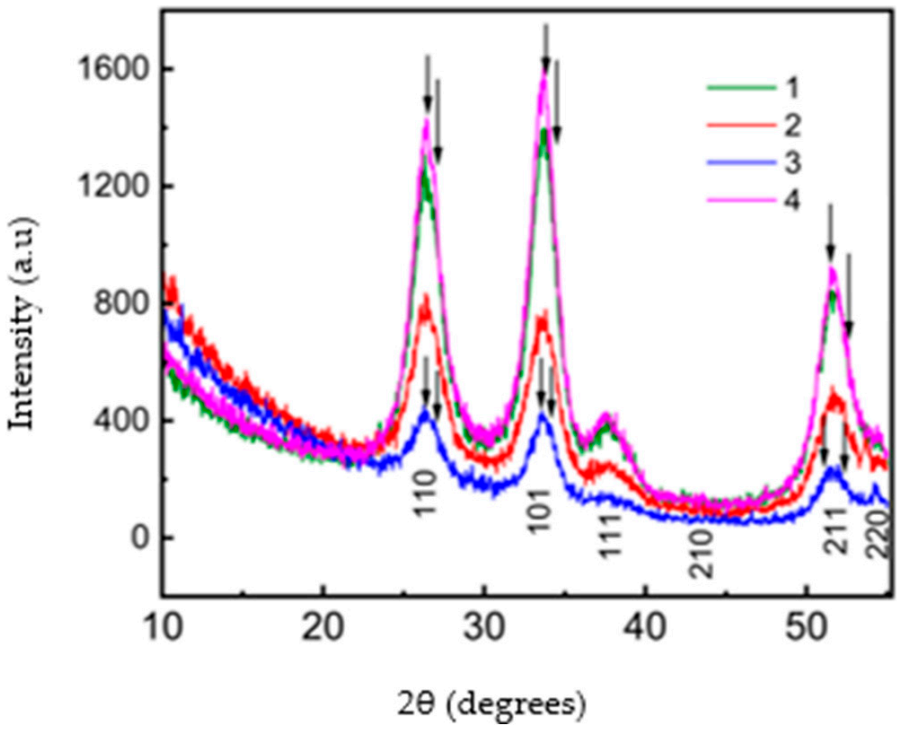


Figure 5. XRD patterns of NGO-containing FTO films: (1) FTO-6; (2) FTO-8; (3) FTO-10; (4) FTO-12. The arrows indicate the positions of peaks corresponding to different phases in the FTO-10 and FTO-12 samples.

These results suggest that the crystal structure of FTO differs between the bulk film and the phase inhomogeneities. The variations in lattice parameters are attributed to the different fluorine content in the tin oxide crystalline matrix. Given that the ionic radius of O^{2-} is smaller than the radius of F^{-} [11], the lattice parameters of the fluorine-depleted phase inhomogeneities are expected to be smaller than those of the bulk layer. The variations in lattice parameters between phases with different fluorine content, as well as the absence in the XRD spectra of peaks corresponding to crystalline phases of Sn, SnO, SnF_2, and Sn_3O_4, indicate that fluorine ions occupy oxygen sublattice positions during the synthesis of the studied films [11,20].

It is noteworthy that the XRD spectra of the FTO-6 and FTO-12 samples predominantly exhibit reflections from the (110) plane, while the spectra of the FTO-8 and FTO-10 samples show reflections from the (101) plane. This signifies that these samples have different preferred crystallographic orientations [11,19]. Moreover, the samples with a preferred (101) orientation demonstrate higher crystalline quality, as evidenced by the greater intensity of the XRD reflections and their smaller full width at half maximum (FWHM).

Importantly, the lattice parameters do not change monotonically with NGO concentration. Nevertheless, for samples sharing the same preferred crystallographic plane, the volume difference between the phases grows with increasing nanographene content.

These results are consistent with the electron microscopy data, demonstrating that increasing the NGO content in the FTO films stimulates phase separation processes leading to the formation of a fluorine-depleted crystalline phase.

A plausible mechanism for the NGO-induced phase separation is proposed as follows: Previous studies indicate that graphene-based nanostructures in polycrystalline SnO_2 and FTO are preferentially localized at crystallite boundaries rather than incorporated into the rutile lattice [23,26]. In the present sol–gel system, the oxygen-containing functional groups on NGO can interact with hydrolyzed tin-containing species and fluorine-containing pre-

cursor species. Such interactions can locally modify precursor condensation, nucleation, and crystallite growth during spray pyrolysis. We therefore propose that NGO-rich regions act as chemically distinct interfacial sites at which part of the fluorine-containing species is adsorbed or retained during film formation, while the surrounding SnO_2:F matrix crystallizes with a different fluorine content. During pyrolytic decomposition, local deoxygenation of NGO and the different thermal decomposition kinetics of the NGO-containing precursor regions may further enhance this compositional contrast. The resulting spatially non-uniform nucleation and fluorine redistribution provide a consistent explanation for the formation of Sn-enriched, fluorine-depleted protrusions and for the increasing difference between the unit-cell volumes of the two rutile-type phases as the NGO concentration increases. This model is consistent with the SEM, EDS, and XRD observations, but it should be regarded as a working hypothesis. Direct verification will require spatially resolved chemical-state analysis, such as XPS mapping or electron-energy-loss spectroscopy, together with in situ studies of precursor decomposition and crystallization.

Figure 6a illustrates the absorption spectra of the analyzed FTO films obtained at room temperature, while Figure 6b presents the corresponding spectra plotted in Tauc coordinates.

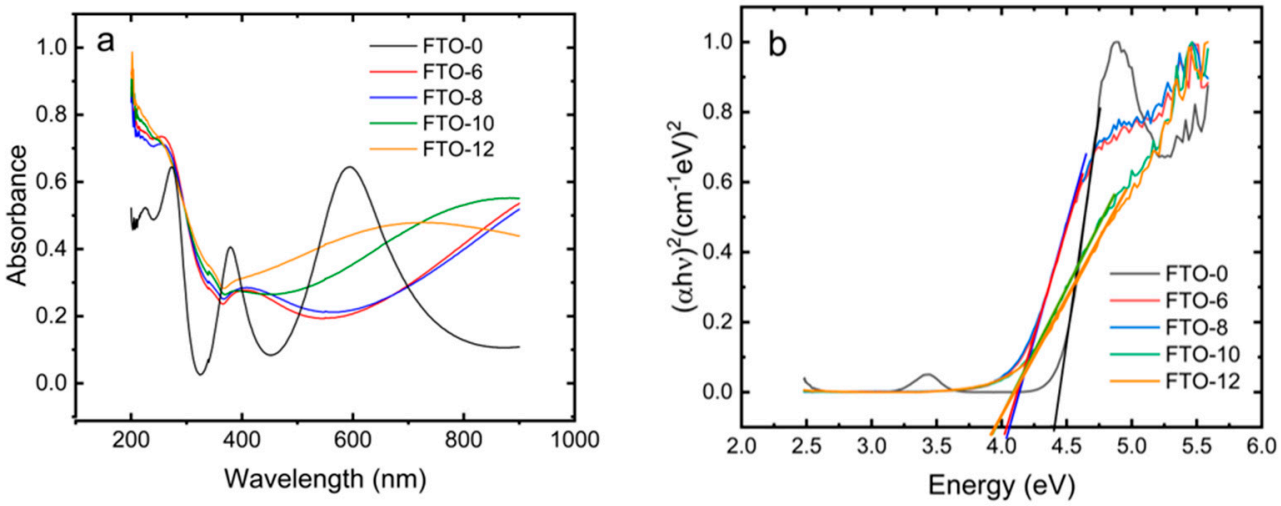


Figure 6. (**a**) Absorbance spectra of the studied FTO layers; (**b**) Tauc plots for the determination of the optical band gap.

The presented spectra reveal that NGO doping significantly modifies the absorbance spectra of the studied FTO layers. The NGO-free FTO-0 sample exhibits pronounced oscillations in absorbance, with maxima at λ = 380 nm and λ = 595 nm. In the NGO-doped samples, these oscillations are substantially weaker. Their peak positions also differ from those in the FTO-0 sample and depend on the NGO concentration. Specifically, an absorption peak appears at λ = 390–420 nm, and its position shifts to shorter wavelengths with increasing NGO content. In the FTO-10 and FTO-12 samples, broad peaks are also observed, with maxima at 875 nm (FTO-10) and 715 nm (FTO-12), respectively. Furthermore, the absorption spectra of the NGO-containing samples suggest the presence of the peak in the range of λ = 340–350 nm.

Notably, oscillations in the optical characteristics are quite typical for transparent conducting oxides. The authors of [25,27] attribute such oscillations to interference between incident waves and waves reflected from the film–substrate interface. However, the peaks in the absorption spectra of the studied samples have irregular positions. This, together with their strong dependence on the NGO content in the FTO layers despite similar film thicknesses, suggests that at least some of the peaks have a different origin. The presence

of absorbing centers is known to induce peaks in the absorbance spectra at frequencies near the natural frequencies of these centers [34,35]. The imaginary part of the complex permittivity, which is responsible for light absorption, is given by:

$$\varepsilon'' = \frac{4\pi\alpha_0\omega\tau N}{1+\omega^2\tau^2} \quad (1)$$

where α_0 is the polarizability, N is the concentration of absorbing centers, τ is the Debye relaxation time (determined by the nature of the absorbing center), and ω is the angular frequency of the electromagnetic radiation. It follows from Equation (1) that the position and intensity of the peaks in the absorption spectra are determined by the parameters and concentration of the absorbing centers. Therefore, we suggest that the observed shift in the peak maxima is related to a change in the nature of the absorbing centers due to phase separation.

Furthermore, we observe that the absorbance in the visible spectral range increases with NGO content. This phenomenon may be attributed to the larger size and higher number of the phase inhomogeneities.

The data presented in Figure 6b demonstrate dependences of the absorption coefficient on the energy of incident photons plotted in Tauc coordinates $(\alpha h\nu)^2$ on the photon energy $h\nu$. In accordance with the Tauc method, a relationship between α and photon frequency ν can be expressed as

$$\alpha h\nu = A\left(h\nu - E_g\right)^n \quad (2)$$

where A is constant, h is a plank constant, E_g is optical band gap, and $n = 1/2$ for FTO which is a direct band semiconductor [11,36]. The band-gap value (E_g) could be estimated by extrapolating the linear part of the curve $(\alpha h\nu)^2$ against ($h\nu$) to the point where $\alpha h\nu = 0$. The least square fit to the linear part of Tauc plot was performed and then extrapolated up to the abscissa. The energy error, determined by least squares method, did not exceed 0.05 eV for each FTO film.

As can be clearly seen from Figure 6b, the NGO doping reduces the optical bandgap determined by the Tauc method. The bandgap decreases from 4.4 eV in the NGO-free FTO-0 sample to 3.95 eV in the FTO-10 and FTO-12 samples, which have the highest NGO content. Sheet resistance (R_{sheet}) measurements for the studied layers show that NGO doping leads to significant (3- to 5-fold) reduction in R_{sheet} compared to undoped FTO layers (Table 3). This indicates that the observed bandgap narrowing cannot be explained by the Burstein–Moss model but is apparently related to changes in the lattice parameters of the FTO matrix during phase separation.

Table 3. Sheet resistance values of FTO samples co-doped with nanographene.

	FTO-0	FTO-6	FTO-8	FTO-10	FTO-12
R_{sheet} (Ω/□)	64,030	14,850	12,450	13,500	18,540

Importantly, the sheet resistance (R_{sheet}) exhibits a non-monotonic dependence on the NGO content in the FTO layer. The lowest R_{sheet} values are observed for the FTO-8 sample, while a further increase in NGO content leads to an increase in R_{sheet}. Let us consider the reasons that determine the effect of NGO doping on the sheet resistance of FTO layers. As demonstrated above, phase separation in NGO-containing FTO layers creates fluorine-depleted phase inhomogeneities. This phenomenon increases the fluorine content and, consequently, raises the charge carrier concentration within the volume of the main layer. However, EDS data indicate that the change in fluorine concentration resulting from phase separation is only tenths of a percent and is insufficient to explain the

significant reduction in sheet resistance. We suggest that the decrease in sheet resistance in NGO-doped samples is primarily due to a change in charge carrier mobility. Indeed, studies [24,27] have reported an increase in charge carrier mobility in SnO_2 and FTO layers doped with graphene and graphene oxide. The authors of [26] ascribe this mobility increase to a reduction in potential barriers and a decrease in the concentration of scattering centers at crystallite interfaces due to the localization of nanographene particles at these interfaces. On the other side, increase in NGO concentration in FTO leads to an increase in the size and number of the phase inhomogeneities. In this case, the rise in sheet resistance in the FTO-10 and FTO-12 samples, which had the highest NGO content, could be explained by a reduction in mobility, that is attributed to enhanced charge carrier scattering at interphases of the phase inhomogeneities [17].

4. Benchmarking Against Related Graphene/SnO_2 and Graphene/FTO Systems

To place the present results in context, Table 4 compares the main electrical and optical outcomes with representative graphene-modified SnO_2 and FTO systems reported in the literature. The comparison must be interpreted with caution because the deposition methods, substrates, film thicknesses, graphene derivatives, and device geometries differ substantially. In particular, carrier mobility was not measured directly in the present study; therefore, the mobility-based explanation proposed above is inferred from the observed sheet-resistance trend and from published transport studies rather than presented as an experimentally determined value.

Table 4. Benchmarking of the present NGO-doped FTO films against representative graphene-modified SnO_2 and FTO systems.

Reference/System	Preparation and Structure	Minimum Sheet Resistance	Carrier Mobility	Optical Bandgap/Principal Optical Result
Present study: NGO-doped FTO	Sol–gel ultrasonic spray pyrolysis; 50 nm films; 0.12–0.24 mol% NGO	12,450 ohm/sq at 0.16 mol% NGO	Not directly measured	Eg decreases from 4.4 to 3.95 eV
Das et al. [25]: rGO-SnO_2	Hydrothermal composite in a Schottky-diode structure	Not reported as film sheet resistance	62% increase relative to SnO_2	Light absorption increased and Eg decreased; absolute Eg not reported in the cited summary
Go et al. [26]: graphene/FTO	Few-layer graphene incorporated during spray pyrolysis	Absolute value not reported in the cited article summary	Not reported	Nearly two-fold increase in transparent-electrode figure of merit, mainly due to lower sheet resistance
Khaleel et al. [28]: graphene/FTO	Spray pyrolysis at 500 °C	8 ohm/sq for optimized G-FTO; 15 ohm/sq for FTO	Not reported	Visible transmittance decreased from 82% to 79% after graphene addition

The benchmarking shows that the minimum sheet resistance obtained here remains substantially higher than that of optimized transparent-electrode FTO films reported by Khaleel et al. [27]. This difference is expected because the present 50 nm layers were

designed to examine NGO-induced structural and compositional changes rather than to reproduce an optimized commercial transparent conductor, and the preparation and measurement configurations differ. Nevertheless, the present work demonstrates a 5.1-fold reduction in sheet resistance relative to the undoped control while simultaneously producing a measurable bandgap reduction of 0.45 eV. Its main contribution is therefore not a record-low absolute sheet resistance, but the experimentally established correlation among NGO concentration, fluorine-depleted phase formation, lattice-parameter splitting, optical-bandgap narrowing, and non-monotonic electrical transport. The mobility enhancement reported for rGO-SnO_2 by Das et al. [24] and the conductivity improvements reported for graphene/FTO systems [25,27] support the plausibility of interface-assisted transport enhancement; however, Hall-effect measurements are required in future work to separate the contributions of carrier concentration and mobility in the present films.

The obtained results indicate that NGO incorporation promotes the formation of fluorine-depleted phase inhomogeneities within the FTO layers. These regions introduce local compositional variations and may act as additional scattering centers for charge carriers. Consequently, the films can be considered as structurally heterogeneous systems in which the main part of the layer retains the conducting FTO matrix, whereas the NGO-associated inhomogeneities modify the local transport pathways.

At moderate NGO concentrations of 0.12–0.16 mol%, the formation of local compositional variations may contribute to the redistribution of fluorine within the film and modify the effective charge-transport pathways, which is consistent with the observed decrease in sheet resistance. However, at higher NGO concentrations of 0.20–0.24 mol%, the increase in the number and size of heterogeneous regions leads to a greater number of interphase boundaries and compositional fluctuations. These structural features may enhance carrier scattering and disrupt continuous transport pathways, thereby contributing to the subsequent increase in sheet resistance.

Thus, macroscopic film uniformity, including a constant thickness and the absence of large defects, is important for the reproducibility of the measured properties, whereas microscopic compositional heterogeneity represents an important factor governing the non-monotonic dependence of the electrical and optical properties on the NGO concentration. The observed results suggest that the properties of the films can be tuned by balancing the beneficial effects of NGO incorporation and local modification of charge-transport pathways against the adverse effects associated with the development of larger and more numerous heterogeneous regions.

Thus, our results show that NGO doping significantly modifies the properties of FTO films. The possibility of obtaining NGO-doped FTO films with controlled properties is of undoubted interest from the point of view of the possibility of using such materials in various fields of photonics and optoelectronics. For example, the discovered dependence of the FTO band gap on the concentration of NGOs can be used for design of selective photodetectors with sensitivity in a given wavelength range. Reducing the resistivity during NGO doping may be of interest from the point of view of using such materials as a bottom electrode in perovskite-based solar cells as well as a top electrode in thin-film solar cells. In each case the optimal concentration of NGOs should be determined based on the goals and objectives of using NGO-doped FTO films. At the same time, taking into account the limited number of studies related to the effect of graphene and its derivatives on the properties of FTO, it seems advisable to conduct additional research in this area. The objective of such studies should be to discover the physical mechanisms that determine the change in the properties FTO films in the NGO doping process, as well as to optimize the technological modes of fabrication and subsequent treatments of NGO-doped FTO films in order to further enhance their characteristics.

The observed relationship between graphene oxide concentration, phase separation, optical bandgap, and electrical conductivity demonstrates that the optical response of NGO-modified FTO films is governed by multiple interacting structural parameters. Recent advances in artificial intelligence and machine learning have shown that data-driven models can successfully predict nonlinear optical properties of graphene-based materials directly from material and excitation parameters, significantly reducing the need for exhaustive experimental optimization [37,38]. Likewise, deep-learning approaches are increasingly being employed for the characterization, prediction, and inverse design of two-dimensional materials and photonic structures. Therefore, the experimental results obtained in this work may serve as a valuable dataset for future machine-learning-assisted optimization of graphene-modified transparent conducting oxides. Such approaches could enable rapid prediction of optical bandgap, absorption spectra, electrical conductivity, and optimal graphene oxide concentration, accelerating the development of transparent electrodes for optoelectronic and photovoltaic devices.

5. Conclusions

Our study has shown that NGO doping leads to significant changes in the structural, optical, and electrophysical properties of FTO layers deposited by spray pyrolysis. NGO doping induces the formation of fluorine-depleted phase inhomogeneities within the FTO bulk, with an increase in NGO content enhancing phase separation. Absorption spectroscopy revealed that both the absorption intensity and the nature of the absorbing centers depend on the NGO content in the FTO layers. The optical bandgap of the FTO layers decreases with increasing NGO content. This decrease is not related to the Burstein–Moss effect but is caused by changes in the lattice parameters of the FTO layer associated with phase separation. NGO doping has been shown to reduce the sheet resistance of the FTO layers, which is attributed to increased charge carrier mobility. The dependence of the sheet resistance on the NGO concentration in the FTO layer is non-monotonic. The increase in sheet resistance at NGO concentrations above 0.16 mol% is associated with enhanced charge carrier scattering at the interfaces of phase inhomogeneities, the concentration of which increases with the level of NGO doping. Our results demonstrate that NGO doping can be used to controllably tune the optical and electrophysical parameters of FTO layers obtained by spray pyrolysis.

This research was supported by the joint Uzbek–Belarusian project “Mechanisms of Formation and Photoelectric Properties of Complex Oxide Films with Tunable Bandgap for the Fabrication of Photosensitive Structures in the Short-Wavelength Range” (registration number in the Republic of Uzbekistan: FL-8824063322; registration number in the Republic of Belarus: BRFFI-T25UZB-111). Peng Li. acknowledges the National Natural Science Foundation of China Grant (Nos. 12461160279, 92365113, 92476204). P.L. acknowledges the support of the State Key Laboratory of Integrated Chips and Systems of Fudan University and the Information Science Laboratory Center of USTC. This work was partially carried out at the USTC Center for Micro and Nanoscale Research and Fabrication.

Author Contributions: Conceptualization, P.P. and A.V.S.; methodology, P.P., S.U.Y. and A.V.S.; validation, A.A.N., P.L., S.A.K. and V.E.G.; formal analysis, P.P., A.V.S. and V.V.S.; investigation, A.A., R.A.N., N.A.K., S.K.S. and K.D.D.; resources, A.A.N., A.V.S. and V.V.S.; data curation, P.P., S.U.Y. and V.V.S.; writing—original draft preparation, P.P. and A.V.S.; writing—review and editing, S.A.K. and A.V.S.; visualization, A.A., R.A.N. and V.V.S.; supervision, P.P. and S.A.K.; project administration, A.A.N., A.V.S. and V.E.G.; funding acquisition, P.P., S.A.K. and P.L. All authors have read and agreed to the published version of the manuscript.

Funding: This research was supported by the joint Uzbek–Belarusian project “Mechanisms of Formation and Photoelectric Properties of Complex Oxide Films with Tunable Bandgap for the

Fabrication of Photosensitive Structures in the Short-Wavelength Range" (registration number in the Republic of Uzbekistan: FL-8824063322; registration number in the Republic of Belarus: BRFFI-T25UZB-111). Peng Li. acknowledges the National Natural Science Foundation of China Grant (Nos. 12461160279, 92365113, 92476204) and the support of the State Key Laboratory of Integrated Chips and Systems of Fudan University and the Information Science Laboratory Center of USTC. This work was partially carried out at the USTC Center for Micro and Nanoscale Research and Fabrication.

Data Availability Statement: Data will be made available on request.

Conflicts of Interest: The authors declare no conflicts of interest.

References

1. Datt, R.; Alsayyed, H.; Dhall, S.; Gupta, S.; Bishnoi, S.; Gupta, R.; Arya, S.; Watson, T.; Tsoi, W.C. Top electrode materials for semi-transparent perovskite solar cells: A review. *Discov. Appl. Sci.* **2025**, *7*, 1348. [CrossRef] [PubMed]
2. He, Y.; Wang, X.; Gao, Y.; Hou, Y.; Wan, Q. Oxide-based thin film transistors for flexible electronics. *J. Semicond.* **2018**, *39*, 011005. [CrossRef]
3. Untila, G.G.; Kost, T.N.; Chebotareva, A.B.; Timofeyev, M.A. Optimization of the deposition and annealing conditions of fluorine-doped indium oxide films for silicon solar cells. *Semiconductors* **2013**, *47*, 415–421. [CrossRef]
4. Wager, J.F. Transparent Electronics. *Science* **2003**, *300*, 1245–1246. [CrossRef] [PubMed]
5. Kang, D.Y.; Kim, B.-H.; Lee, T.H.; Shim, J.W.; Kim, S.; Sung, H.-J.; Chang, K.J.; Kim, T.G. Dopant-Tunable Ultrathin Transparent Conductive Oxides for Efficient Energy Conversion Devices. *Nano-Micro Lett.* **2021**, *13*, 211. [CrossRef] [PubMed]
6. Aksenova, V.V.; Smirnova, I.P.; Markov, L.K.; Pavlyuchenko, A.S.; Yagovkina, M.A. Effect of oxygen on the formation process of nanostructured indium-tin oxide films. *Phys. Solid State* **2023**, *65*, 2079. [CrossRef]
7. Khan, M.Z.H. Pretreatment of ITO Electrode and Its Physiochemical Properties:Towards Device Fabrication. *Surf. Eng. Appl. Electrochem.* **2016**, *52*, 547–564. [CrossRef]
8. Kudryashov, D.A.; Maksimova, A.A.; Vyacheslavova, E.A.; Uvarov, A.V.; Morozov, I.A.; Baranov, A.I.; Monastyrenko, A.O.; Gudovskikh, A.S. Study of the influence of the design features of a magnetron sputtering system on the electrical and optical properties of indium-tin oxide films. *Semiconductors* **2021**, *55*, 360. [CrossRef]
9. Deng, W.; Ohgi, T.; Nejo, H.; Fujita, D. Characteristics of Indium Tin Oxide Films Deposited by DC and RF Magnetron Sputtering. *Jpn. J. Appl. Phys.* **2001**, *40*, 3364. [CrossRef]
10. Saehana, S.; Siswomiharjo, D.; Aprilia, A. Investigation of experimental parameters in fabrication of Fluorine-doped Tin Oxide (FTO) using spray pyrolysis. *Int. J. Heat Technol.* **2025**, *43*, 1076–1084. [CrossRef]
11. Kumar, K.D.A.; Valanarasu, S.; Jeyadheepan, K.; Kim, H.-S.; Vikraman, D. Evaluation of the physical, optical, and electrical properties of SnO_2: F thin films prepared by nebulized spray pyrolysis for optoelectronics. *J. Mater. Sci. Mater. Electron.* **2018**, *29*, 3648–3656. [CrossRef]
12. Kafle, M.; Kapadi, R.K.; Joshi, L.P.; Rajbhandari, A.; Subedi, D.P.; Gyawali, G.; Lee, S.W.; Adhikari, R.; Kafle, B.P. Effect of calcination environments and plasma treatment on structural, optical and electrical properties of FTO transparent thin films. *AIP Adv.* **2017**, *7*, 075101. [CrossRef]
13. Cid, C.P.; Spada, E.; Sartorelli, M. Effect of the cathodic polarization on structural and morphological proprieties of FTO and ITO thin films. *Appl. Surf. Sci.* **2013**, *273*, 603–606. [CrossRef]
14. Tran, Q.-P.; Fang, J.-S.; Chin, T.-S. Propertiesof fluorine-doped SnO_2 thin films by a green sol–gel method. *Mater. Sci. Semicond. Process.* **2015**, *40*, 664–669. [CrossRef]
15. Benhaoua, A.; Rahal, A.; Benhaoua, B.; Jlassi, M. Effect of fluorine doping on the structural, optical and electrical properties of SnO_2 thin films prepared by spray ultrasonic. *Superlattices Microstruct.* **2014**, *70*, 61–69. [CrossRef]
16. Dai, X.; Koshy, P.; Sorrell, C.C.; Lim, J.; Yun, J.S. Focussed Review of Utilization of Graphene-Based Materials in Electron Transport Layer in Halide Perovskite Solar Cells: Materials-Based Issues. *Energies* **2020**, *13*, 6335. [CrossRef]
17. Ramaiah, K.S.; Raja, V.S. Structural and electrical properties of fluorine doped tin oxide films prepared by spray-pyrolysis technique. *Appl. Surf. Sci.* **2006**, *253*, 1451–1458. [CrossRef]
18. Agashe, C.; Hüpkes, J.; Schöpe, G.; Berginski, M. Physical properties of highly oriented spray-deposited fluorine-doped tin dioxide films as transparent conductor. *Sol. Energy Mater. Sol. Cells* **2009**, *93*, 1256–1262. [CrossRef]
19. Banyamin, Z.Y.; Kelly, P.J.; West, G.; Boardman, J. Electrical and Optical Properties of Fluorine Doped Tin Oxide Thin Films Prepared by Magnetron Sputtering. *Coatings* **2014**, *4*, 732–746. [CrossRef]
20. Pinheiro, X.; Vilanova, A.; Mesquita, D.; Monteiro, M.; Eriksson, J.; Barbosa, J.; Matos, C.; Oliveira, A.; Oliveira, K.; Capitão, J.; et al. Design of experiments optimization of fluorine-doped tin oxide films prepared by spray pyrolysis for photovoltaic applications. *Ceram. Int.* **2023**, *49*, 13019–13030. [CrossRef]

21. Thomas, R.; Mathavan, T.; Ganesh, V.; Yahia, I.S.; Zahran, H.Y.; AlFiafy, S.; Kathalingam, A. Investigation of erbium co-doping on fluorine doped tin oxide via nebulizer spray pyrolysis for optoelectronic applications. *Opt. Quantum Electron.* **2020**, *52*, 248. [CrossRef]
22. Khakhomov, S.; Semchenko, A.; Sidski, V.; Gaishun, V.; Kovalenko, D.; Maevsky, A.; Danilchenko, K.; Parchinskiy, P. Electrophysical and Optical Characteristics of thin Doped FTO Films for Optoelectronics and Photovoltaics. In *Proceedings of the 2025 9th International Conference on Information, Control, and Communication Technologies, ICCT 2025 Gomel, Belarus*; IEEE: New York, NY, USA, 2025; pp. 1–4.
23. Abdulzahraa, H.G.; Mohammed, M.K.; Raoof, A.S.M. Tin oxide/reduced graphene oxide hybrid as a hole blocking layer for improving 2D/3D hetrostructured perovskite-based photovoltaics. *Surf. Interfaces* **2022**, *31*, 102092. [CrossRef]
24. Das, P.; Pal, B.; Datta, J.; Das, M.; Sil, S.; Ray, P.P. Improved charge transport properties of graphene incorporated tin oxide based Schottky diode over pure one. *J. Phys. Chem. Solids* **2021**, *148*, 109706. [CrossRef]
25. Go, L.; Macaraig, L.; Enriquez, E. Few-layer-graphene as intercalating agent for spray-pyrolysed fluorine-doped tin oxide transparent conducting electrode. *Bull. Mater. Sci.* **2020**, *43*, 65. [CrossRef]
26. Cai, W.; Wang, L.; Wang, L.; Wang, G.; Yu, J.; Zhao, H. Preparation of Fluorine-doped Tin Oxide-Graphene Composite Films and Study of Its Structure and Properties. *J. Chin. Ceram. Soc.* **2019**, *47*, 1484–1490. [CrossRef]
27. Khaleel, S.A.; Shaban, M.; Alsharekh, M.F.; Hamad, E.K.I.; Shehata, M.I.M. Preparation and characterization of graphene-based fluorine doped tin dioxide thin films via spray pyrolysis technique. *J. Electr. Eng.* **2023**, *74*, 463–473. [CrossRef]
28. Gracia, L.; Beltran, A.; Andres, J. Characterization of the High-Pressure Structures and Phase Transformations in SnO_2. A Density Functional Theory Study. *J. Phys. Chem. B* **2007**, *111*, 6479–6485. [CrossRef] [PubMed]
29. Ahmed, A.S.; Azam, A.; Shafeeq, M.M.; Chaman, M.; Tabassum, S. Temperature dependent structural and optical properties of tin oxide nanoparticles. *J. Phys. Chem. Solids* **2012**, *73*, 943–947. [CrossRef]
30. Seki, H.; Ishizawa, N.; Mizutani, N.; Kato, M. High-Temperature Structures of the Rutile-Type Oxides TiO_2 and SnO_2. *Yogyo Kyokai Shi—J. Ceram. Soc. Jpn.* **1984**, *92*, 219–223.
31. Haines, J.; Leger, J.M. X-ray diffraction study of the phase transitions and structural evolution of tin dioxide at high pressure: Relationships between structure types and implications for other rutile-type dioxides. *Phys. Rev. B* **1997**, *55*, 11144–11154. [CrossRef]
32. Taylor, D. Thermal expansion IV. Binary oxides with the silica structures. *Trans. J. Br. Ceram. Soc.* **1984**, *83*, 129–134.
33. Mani, A. X-ray characterization of chemical vapour-deposited SnO_2. *J. Mater. Sci. Lett.* **1990**, *9*, 1106–1108. [CrossRef]
34. Kittel, C. *Introduction to Solid State Physics*, 8th ed.; Wiley: Hoboken, NJ, USA, 2013; p. 680.
35. Lee, M. *Optics for Materials Scientists Toronto*; Apple Academic Press: Point Pleasant, NJ, USA, 2020.
36. Tomaev, V.V.; Sokhovich, E.V.; Myakin, S.V.; Polishchuk, V.A.; Semenova, A.A. Obtaining and Studying Films of Tungsten, Titanium and Their Oxides. *Glass Phys. Chem.* **2022**, *48*, 61–68. [CrossRef]
37. García-Córdova, J.Z.; Arano-Martinez, J.A.; Mercado-Zúñiga, C.; Martínez-González, C.L.; Torres-Torres, C. Predicting the Multiphotonic Absorption in Graphene by Machine Learning. *AI* **2024**, *5*, 2203–2217. [CrossRef]
38. Meng, X.; Qin, C.; Liang, X.; Zhang, G.; Chen, R.; Hu, J.; Yang, Z.; Huo, J.; Xiao, L.; Jia, S. Deep learning in two-dimensional materials: Characterization, prediction, and design. *Front. Phys.* **2024**, *19*, 53601. [CrossRef]

Disclaimer/Publisher's Note: The statements, opinions and data contained in all publications are solely those of the individual author(s) and contributor(s) and not of MDPI and/or the editor(s). MDPI and/or the editor(s) disclaim responsibility for any injury to people or property resulting from any ideas, methods, instructions or products referred to in the content.